Applied Radiation and Isotopes 68 (2010) 1687–1693

Contents lists available at ScienceDirect

Applied Radiation and Isotopes

journal homepage: www.elsevier.com/locate/apradiso

# Use of synchrotron-based diffraction-enhanced imaging for visualization of soft tissues in invertebrates

Donepudi V. Rao [a,*], Medasani Swapna [a,1], Roberto Cesareo [a], Antonio Brunetti [a], Zhong Zhong [b], Takao Akatsuka [c], Tetsuya Yuasa [c], Tohoru Takeda [d], Giovanni E. Gigante [e]

[a] Istituto di Matematica e Fisica, Università degli Studi di Sassari, Via Vienna 2, 07100 Sassari, Italy
[b] National Synchrotron Light Source, Brookhaven National Laboratory, Upton, NY 11973, USA
[c] Department of Bio-System Engineering, Faculty of Engineering, Yamagata University, Yonezawa-shi, Yamagata-992-8510, Japan
[d] Allied Health Science, Kitasato University 1-15-1 Kitasato, Sagamihara, Kanagawa 228-8555, Japan
[e] Dipartimento di Fisica, Universita di Roma, La Sapienza, 00185 Roma, Italy

ARTICLE INFO

*Article history:*
Received 19 June 2008
Received in revised form
4 April 2010
Accepted 4 April 2010

*Keywords:*
Diffraction-enhanced imaging
Synchrotron
Invertebrates
Soft tissue

ABSTRACT

Images of terrestrial and marine invertebrates (snails and bivalves) have been obtained by using an X-ray phase-contrast imaging technique, namely, synchrotron-based diffraction-enhanced imaging. Synchrotron X-rays of 20, 30 and 40 keV were used, which penetrate deep enough into animal soft tissues. The phase of X-ray photons shifts slightly as they traverse an object, such as animal soft tissue, and interact with its atoms. Biological features, such as shell morphology and animal physiology, have been visualized. The contrast of the images obtained at 40 keV is the best. This optimum energy provided a clear view of the internal structural organization of the soft tissue with better contrast. The contrast is higher at edges of internal soft-tissue structures. The image improvements achieved with the diffraction-enhanced imaging technique are due to extinction, i.e., elimination of ultra-small-angle scattering. They enabled us to identify a few embedded internal shell features, such as the origin of the apex, which is the firmly attached region of the soft tissue connecting the umbilicus to the external morphology. Diffraction-enhanced imaging can provide high-quality images of soft tissues valuable for biology.



## 1. Motivation

In studies of the structural organization of terrestrial and marine invertebrates, such as snails and bivalves, it is important to visualize organs and complex internal features. The organisms of these groups are excellent models useful for better understanding of living systems. It is difficult to obtain high-contrast X-ray images of the soft tissues of these organisms with conventional methods because the X-ray absorption coefficients of the light elements, which constitute the soft tissues, are small. As a result, the soft tissues are relatively transparent for X-rays, and the contrast is poor. The problem of insufficient contrast of soft tissues is typically overcome by using lower-energy X-rays, but, because of the dense outer shell, this is not a feasible solution for imaging of such objects. The contrast in X-ray images of soft tissues can also be improved by effective monochromatization. Such monochromatization is provided, in particular, in synchrotron-based diffraction-enhanced imaging, one of the X-ray phase-contrast imaging techniques.

Synchrotron sources provide beams with intensities of many orders of magnitude higher than the intensities of X-rays from conventional X-ray tubes. Synchrotron radiation is characterized by high collimation (small angular divergence of the beam), low emittance (the product of source cross-section and solid angle of emission is small), wide range of energies/wavelengths available with monochromatization (from below 1 eV up to several MeV), high level of polarization (linear or elliptical), and pulsed light emission (pulse durations at or below 1 ns). The combination of the high flux and low divergence achievable with synchrotron sources was crucial to the great success of experiments in synchrotron-based soft-tissue X-ray imaging. Due to the high intensity of synchrotron beams, the flux of photons transmitted through the sample is much higher than in the case of an X-ray tube source, and the produced images have better contrast (Rao et al., 2003a).

## 2. Diffraction-enhanced imaging

The behavior of X-rays traversing a sample can be described with a complex index of refraction, just like in the conventional

* Corresponding author. Present address: Department of Physics, Sir CRR Autonomous College, Eluru-534007, W.G.Dt., AP, India.
*E-mail addresses:* donepudi_venkateswararao@rediffmail.com (D.V. Rao), medasanisw@gmail.com (M. Swapna).
[1] Present address: Department of Physics, Sri Durga Malleswari Siddhartha Mahila Kalasala, Bunder Road, Vijayawada 520010, Krishna Dt., AP, India.

0969-8043/$ - see front matter © 2010 Elsevier Ltd. All rights reserved.
doi:10.1016/j.apradiso.2010.04.001

optics. In the X-ray region, the index of refraction $n$ deviates from unity only slightly and can be expressed as $1-\delta-i\beta$, where $\beta$ describes the absorption of X-rays and the phase-shift term $\delta$ represents refractive effects.

Diffraction-enhanced imaging derives contrast from absorption, refraction and extinction. The real and imaginary parts of the refractive indices are responsible for the phase shifts and absorption resulting in enhanced contrast imaging. For biological samples, the real part is up to 1000 times greater than the imaginary part, which makes phase-sensitive imaging techniques more effective than conventional methods. Important advantages of X-ray refraction over X-ray absorption were found recently in some imaging applications. Refraction provides one-to-two orders of magnitude higher sensitivity, particularly in the case of biological and other low-$Z$ materials. Diffraction-enhanced imaging technique with highly collimated synchrotron X-rays takes advantage of these refraction properties to differentiate between similar biological soft tissues (Fitzgerald, 2000; Wilkins et al., 1996).

Diffraction-enhanced X-ray imaging (DEI) makes use of the combination of absorption, refraction and scatter rejection, which enables one to visualize small differences in tissue densities with X-rays (Chapman et al., 1997). This new X-ray imaging technology implemented at the National Synchrotron Light Source (NSLS) at Brookhaven National Laboratory (USA) is able to visualize breast tissue and other similar biological tissues (Zhong et al., 1997; Chapman et al., 1998; Muehleman et al., 2003; Oltulu et al., 2003; Li. et al., 2003; Lewis et al., 2003; Kiss et al., 2004).

High-intensity synchrotron X-rays are presently finding many applications, and techniques are being rapidly developed that can detect X-ray phase shifts within soft tissues. DEI was used to image rat bone and lumber vertebra (Rao et.al., 2005), rat spine (Kelly et al., 2006), cartilage damage (Muehleman et al., 2006a), effects of ophthalmic diseases (Antunes et al., 2006)) and controlled defects within bone, including bone–metal gaps (Connor et al., 2006). There are also publications on using wide-beam source in DEI (Kim et al., 2006), mass density imaging (Wernick et al., 2006), multiple-image radiography (Khelashvili et al., 2006; Brankov et al., 2006; Muehleman et al., 2006b; Chou et al., 2007), compositional images (Hasnah et al., 2007), images of seeds (Young et al., 2007) and images of biological soft tissues (Rao et al., 2007). In the last few years, the diffraction-enhanced imaging system at NSLS beamline X15A was upgraded with new optics, electronics, mechanics and software. The quality of images of phantoms and real biological samples has been steadily improving (Hasnah and Chapman, 2008; Kelly et al., 2007). These studies suggest that diffraction-enhanced imaging is a potent, valuable and reliable tool for studying the refraction and scattering properties of objects. Furthermore, because relatively high-energy X-rays are used, X-ray absorption is weak, and the resulted radiation damage is small.

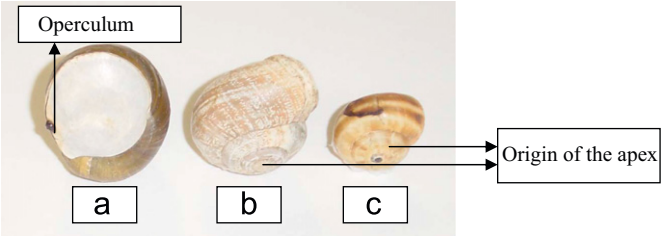


**Fig. 1.** (a) A round snail (local name *Monzette*), 20 mm in diameter, (b) and (c) two snails of type *Helix aspersa,* diameters 20 and 10 mm.

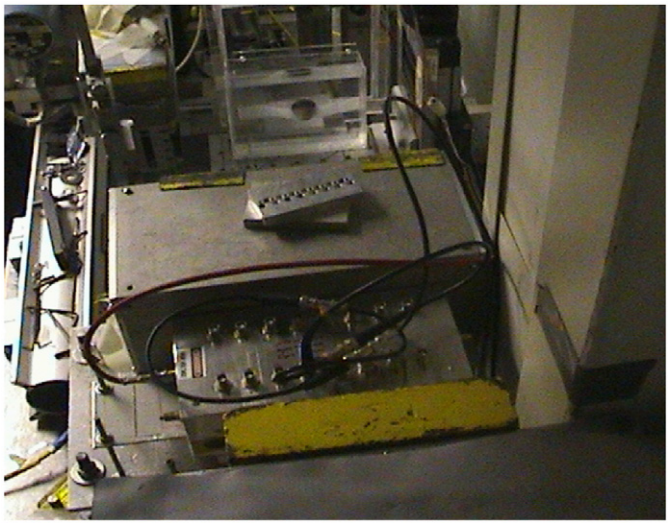

**Fig. 3.** Experimental setup. Samples are fixed in the middle of the Perspex containers with water.

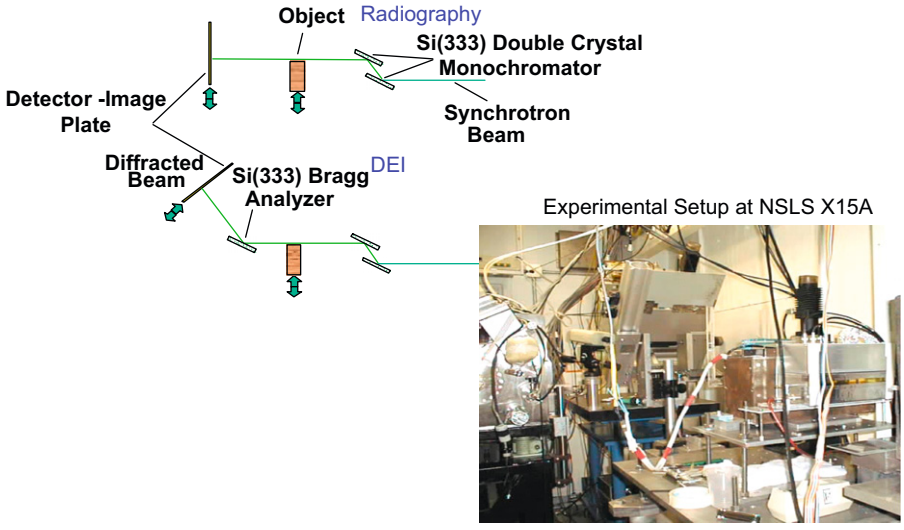


**Fig. 2.** Synchrotron radiography and DEI system, with the associated electronics, used for the acquisition of the images at X-15 A, NSLS, BNL, USA.

### 2.1. Specimens

Fresh samples of terrestrial (snails) and marine (bivalves) invertebrates of various sizes, which contained considerable amounts of biological soft tissue, were collected in winter before spawning to maximize the biomass. The samples were packed in Teflon containers and stored in cold water. Before the acquisition of the images, they were checked for any leakage of the soft tissue from the boundaries of the shells (Rao et al., 2003b). The soft tissue goes out of the apex when the animal moves. The movement of the animal was minimal because the sample was in cold water. In addition, the water bath ensured a more uniform distribution of the X-ray absorption in the sample and container. Fig. 1 shows the shape of the samples used in the experiments. Two snails (type Helix aspersa) of different diameters (10 and 20 mm) and a round snail (locally known as Monzette) of 20-mm diameter were used. These snails had 5–10 mm of the embedded soft tissue depending on the snail size.

## 3. Materials and methods

Details of the diffraction-enhanced imaging technology and the associated instrumentation have been presented previously (Zhong et al., 1997; Zhong et al., 2000). Fig. 2 shows a diagram of the diffraction-enhanced imaging system used in our experiments at the X15A beamline of NSLS. The highly collimated beam of X-rays was produced by a Si(3 3 3) monochromator consisting of two perfect silicon crystals. Once this beam passed through the object, a third crystal (analyzer crystal) of the same reflection index diffracted the X-rays onto a radiographic film (Kodak Professional Industrie 150, Industrex SR45) or an image plate detector (Fuji HRV image plate, read out by a Fuji BAS2500 image plate reader). The distance between the X-ray source and the specimen was approximately 20 m, while the distance between the specimen and the X-ray film or the image plate detector was 1 m. The image of the object was produced by scanning the object and X-ray film at the same speed through the fan beam in approximately opposite directions to take account of the Bragg reflection by the analyzer crystal. Due to the non-dispersive nature of the crystals, the small Darwin width of the diffraction, and the short distance between the sample and the detector, the resolution of the image was limited by the resolution of the X-ray film (50 μm).

The Bragg condition in the analyzer crystal is met only when the incident beam makes the correct angle with the lattice planes in the crystal specific for a given X-ray energy. When this is the case, the beam diffracts from the planes over a narrow range of incident angles. As the analyzer crystal is rotated about the horizontal axis, the crystal will go through the Bragg condition for diffraction, and the diffracted intensity will trace out a profile or a rocking curve. The rocking curve of the analyzer in the protocol described here is roughly triangular and has peak reflectivity close to unity. The width of this profile is typically a few microradians (the full width at half maximum is 1.5 μrad at 40 keV and 3.6 μrad at 18 keV, if the Si(3 3 3) reflection is used). Due to this small angular width, it is possible to analyze, on the microradian scale, the angles of X-ray beams modified by the traversed object. As the

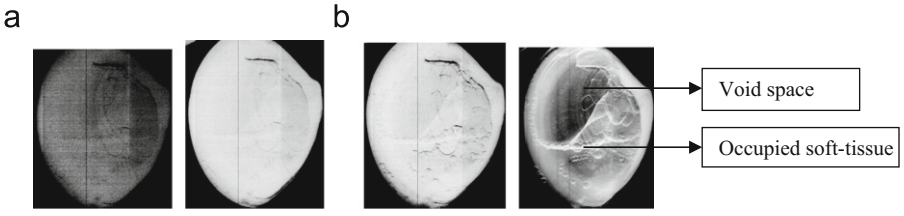


**Fig. 4.** Diffraction-enhanced images of a bivalve at 20 keV: (a) absorption and (b) refraction.

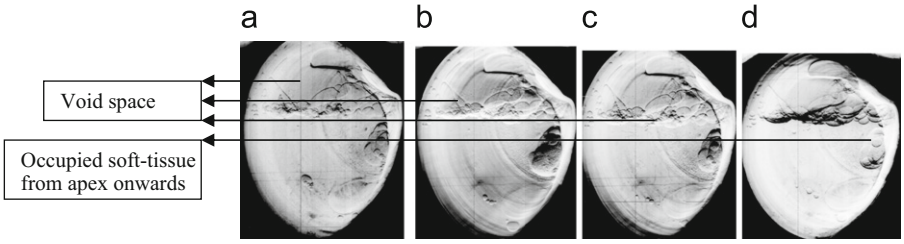


**Fig. 5.** Diffraction-enhanced images of the bivalve at 30 keV with improved contrast at the beginning of the apex at different orientations of the sample. The void space seen in images (a)–(c) and dense soft tissue seen in image (d).

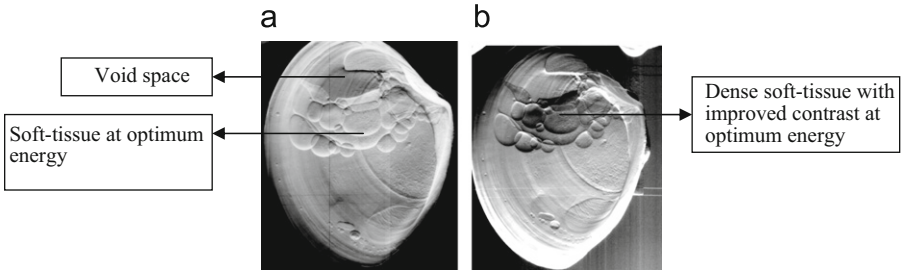


**Fig. 6.** Diffraction-enhanced images of a bivalve at 40 keV with improved contrast at the beginning of the apex (a) and boundaries (b).

range of the angles that can be accepted by the analyzer crystal is only a few microradians, the analyzer crystal detects the X-ray scattering (ultra-small-angle scattering) and refraction of X-rays from the object at the microradian level with angular sensitivity unachievable in conventional radiography. In order to extract refraction information, the analyzer crystal is typically set to the half-intensity points on the low- and high-angle sides of the rocking curve (referred to as $-1$ and $+1$, respectively) or to the points at the base of the rocking curve (referred to as $-2$ and $+2$, respectively) for the low- and high-angle sides during image acquisition. For optimal extinction (scatter rejection) sensitivity, the analyzer crystal is typically set to the peak of the rocking

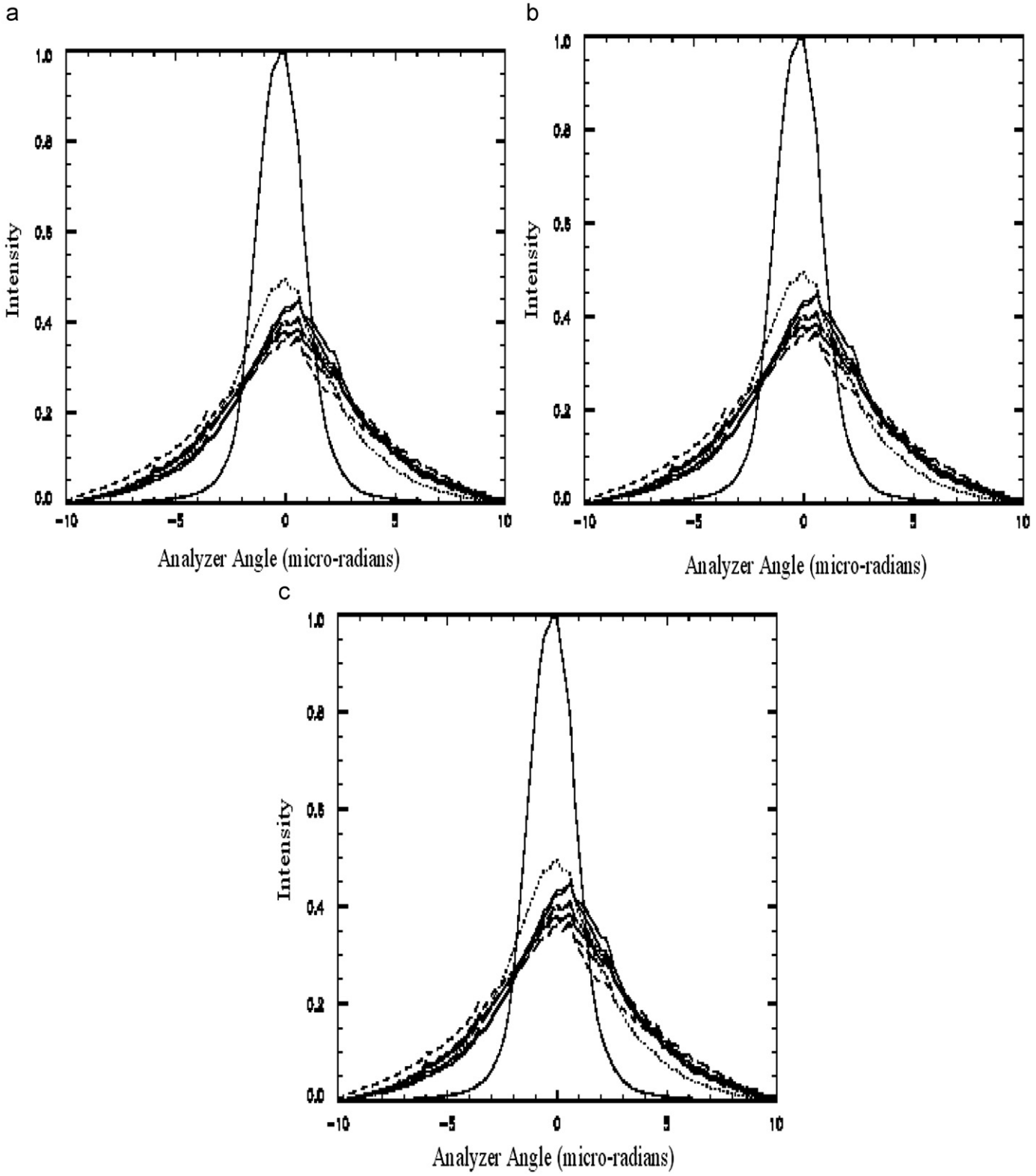


**Fig. 7.** Rocking curves for bivalves at (a) 20 keV, (b) 30 keV and (c) 40 keV. The sharp peak is from air and the broadened ones are from the sample.

curve. In addition, if two images are taken on the steepest slope of the reflectivity, so-called absorption image and refraction image can be calculated. Diffraction-enhanced imaging relies on images recorded at well-known positions on the reflectivity curve of the analyzer crystal.

The reproducibility of diffraction-enhanced images is provided by checking the intensity of the X-rays diffracted by the analyzer crystal just prior to imaging to make sure that the analyzer crystal is in the prescribed angular position. Fig. 3 shows a diffraction-enhanced imaging system with a sample. All specimens were imaged in a medial-to-lateral direction at 20, 30 and 40 keV using diffraction-enhanced imaging and conventional synchrotron X-ray radiography with the analyzer crystal removed and the object scanned through the monochromatic fan beam (at the same X-ray energy and the same X-ray dose as in diffraction-enhanced imaging).

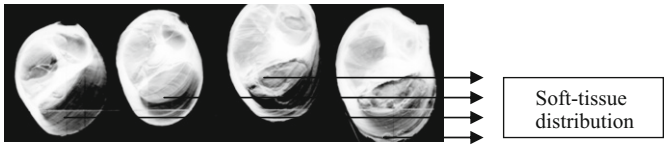


**Fig. 8.** Diffraction-enhanced images of small snails of different shapes taken at 20 keV, focusing the apex. The orientation of the soft tissue is partially visible.

## 4. Results and discussion

### 4.1. Diffraction-enhanced image analysis

Bivalve diffraction-enhanced images acquired at 20, 30 and 40 keV are shown in Figs. 4–6. Figs. 4a and b show absorption and refraction images of marine bivalves obtained at 20 keV. We used a data set of 22 images obtained at various analyzer settings. The images clearly depict anatomical features of the embedded soft tissues and the void space adjacent to the external hard shell. Figs. 5 and 6 show similar images obtained at 30 and 40 keV.

An analysis of these images in relation to their energies prompted us to use contrast agents (such as water) for choosing the optimal energy providing better visualization of the embedded soft-tissue distribution within the shell. The contrast in the diffraction-enhanced images (Figs. 5a–d) represents differences in intensity scattered at a particular angle. At 40 keV, we acquired images at various orientations of the objects. The contrast was considerably higher than in the images acquired at 20 and 30 keV. The diffraction-enhanced images show that the bivalves are joined by a hinge along the length of the body on the dorsal side. There was some decomposition of the soft tissue in the process of image acquisition seen in the form of bubbles. These shells have elastic ligaments (strips between the valves, which prevent loss of biomass) (Fig. 6b).

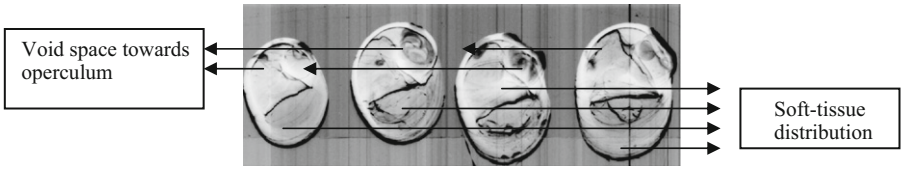


**Fig. 9.** Same as in Fig. 8 but at 30 keV, focusing beam towards operculum. The void space and the associated soft tissue are visible.

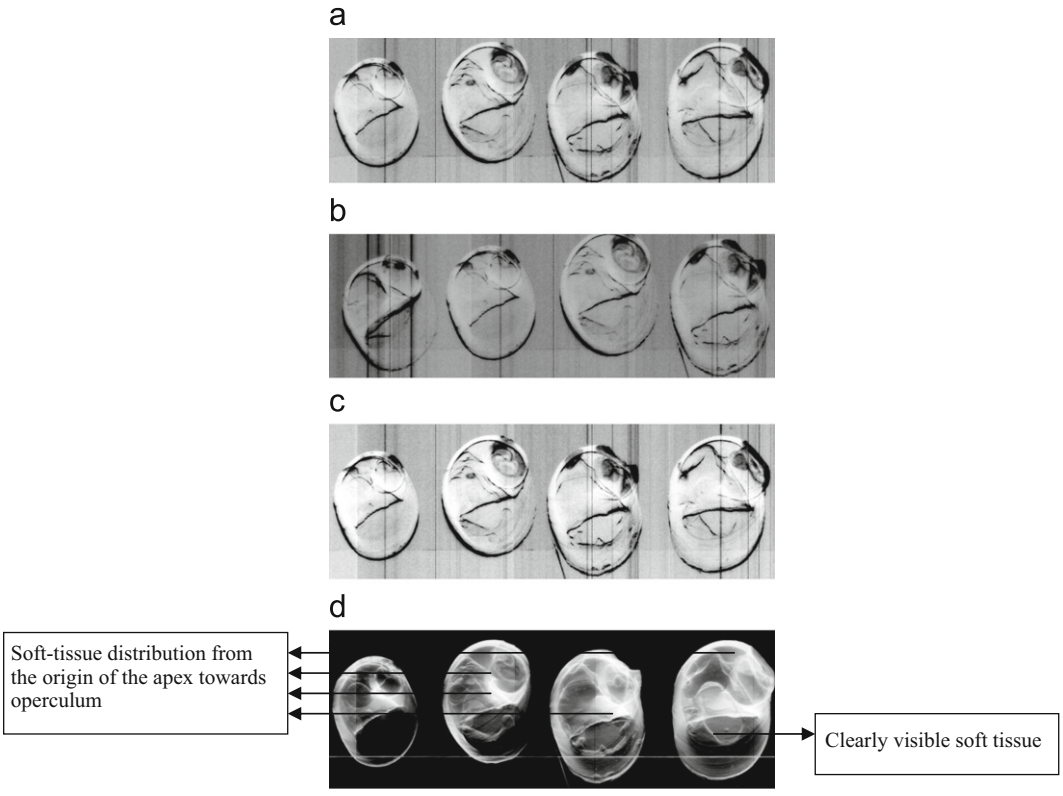


**Fig. 10.** (a)–(d) same as in Fig. 8, but taken at 40 keV.

The rocking curve of the analyzer crystal characterizes the angular sensitivity of the diffraction-enhanced imaging system. A rocking curve scan was performed with the beam across the embedded soft tissue. A rocking curve is sensitive to the microradian alterations in the direction of the incident beam resulted from the changes in the refractive index within soft tissues. In diffraction-enhanced imaging, two images at the opposite sides of the rocking curve are combined on a pixel-by-pixel basis to obtain a single image containing both the refraction and the absorption information. Fig. 7 shows rocking curve of the bivalves with the embedded biological soft tissue obtained at 20, 30 and 40 keV through the specific regions of interest and the peak position of the rocking curve. The sharp peak is the analyzer's rocking curve with the beam passing outside the sample, through air. The other rocking curves are through the shell, and they correspond to a typical region of the embedded soft tissue, including the soft tissue within the two valves, i.e., front and back, and other body tissues. To account for the absorption of X-rays, the rocking curves were normalized so that the area under each rocking curve was equal to the integrated reflectivity of the analyzer measured through the air. In the diffraction-enhanced peak image, the external shell and the soft tissue are less dense, while the X-rays passing through the external shell and the soft tissue are more intense. The considerable contrast gain for external shell and the embedded biological soft tissue reflect the sensitivity and soft-tissue specificity of the diffraction-enhanced imaging system, which are not typical of the conventional radiography.

Figs. 8–10 show the diffraction-enhanced images of a smaller snail in the regions of apex, operculum and soft tissue, which were obtained at 20, 30 and 40 keV. Figs. 10a–d demonstrate that the contrast improves with increasing energy. At 40 keV, the contrast and the visibility of the soft-tissue shape are reasonably acceptable (Fig. 10d). Fig. 11 shows an image of a larger snail obtained at 40 keV. The internal anatomical features are clearly visible here, and the contrast is much better than in the images obtained at the other energies. We have chosen this energy to image the soft tissue without the shell. The magnified regions of the diffraction-enhanced image with reliable diagnostic shell features are shown in Fig. 11.

Fig. 12 shows a diffraction-enhanced image of the soft tissue in water obtained at 20, 30 and 40 keV. Diffraction-enhanced images

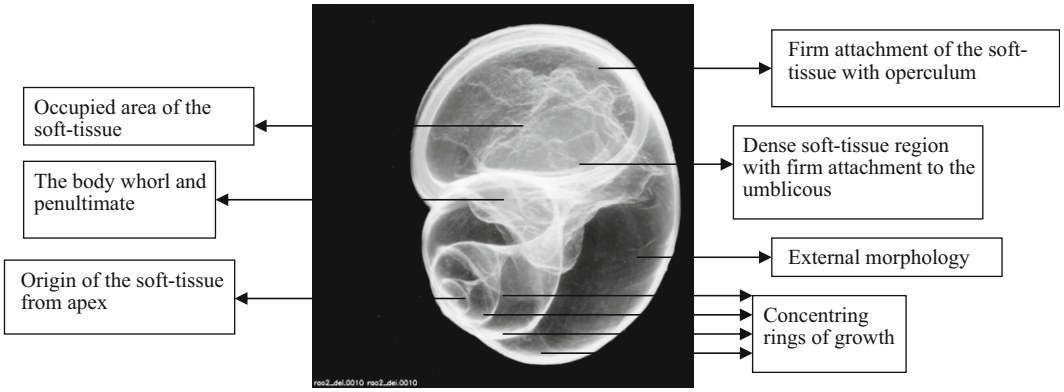


**Fig. 11.** Diffraction-enhanced image obtained at 40 keV, showing the anatomical architecture of apex and interior soft-tissue features with operculum attachment. No leakage of the soft tissue from the boundaries.

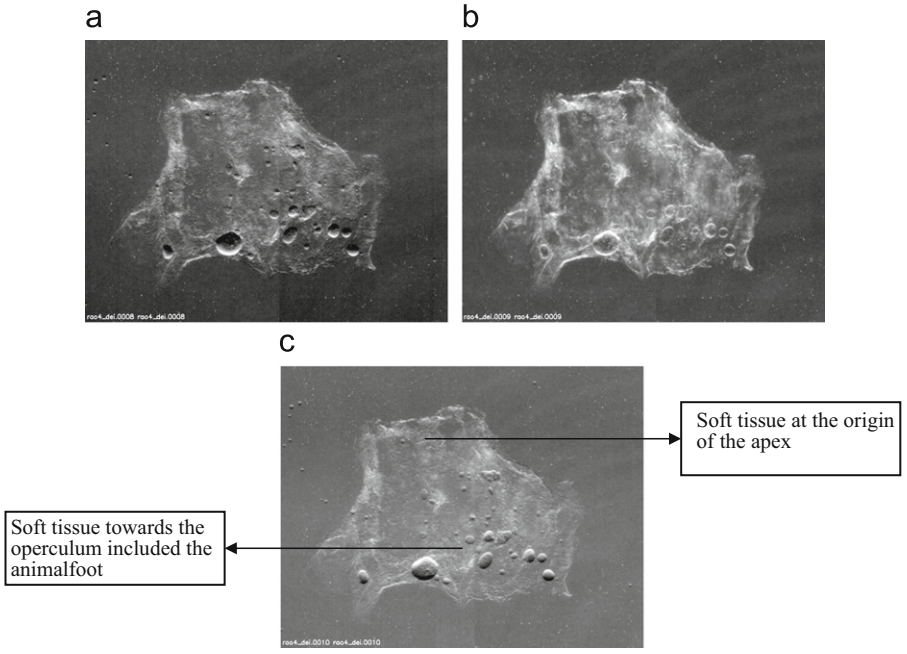


**Fig. 12.** Diffraction-enhanced images of the soft tissue (taken from a larger snail) obtained in water at (a) 20 keV, (b) 30 keV and (c) 40 keV with improved contrast from the origin of the apex towards operculum.

obtained at the top of the rocking curve have contrast from ultra-small-angle scattering, refraction and pure absorption. The internal features are clearly visible in all these images, but the contrast at 40 keV is higher. The 40-keV images provided unique views (Fig. 12c) and demonstrated high sensitivity of the method to low-absorbing structures, which normally produce very poor contrast in conventional radiography. For example, diffraction-enhanced imaging has visualized the attachment of the soft tissue to the umblicuous, highlighting the barrier between the soft tissue and the elastic strip. This became possible as a result of studying factors affecting the contrast and choosing optimal energy. With this method and optimal parameters, weakly-attenuating soft tissue can be differentiated from strongly-attenuating hard shell.

## 5. Conclusion

At the optimum energy, the morphogenetic features in the external shell and certain features of the internal anatomy are clearly visible. Further improvements of imaging of soft tissues of these small animals will provide new information useful for biology, paleontology and marine geology.

## Acknowledgements

One of the authors (DVR) utilized the available facilities at ICTP (Trieste, Italy), Istituto di Matematica e Fisica, Universita di Sassari, Italy, and Department of Bio-System Engineering of Yamagata University (Yonezawa, Japan). Travel support (DVR) at the time of experiments was supported by DST, India, under the category of utilization of synchrotron and neutron scattering facilities.

## References

Antunes, A., Safatle, A., Barros, P., Morelhao, S., 2006. X-ray imaging in advanced studies of ophthalmic diseases. Med. Phys. 33, 2338–2343.

Brankov, J.G., Wernick, M.N., Yang, Y., Li, J., Muehleman, C., Zhong, Z., Anastasio, M., 2006. A computed tomography implementation of multiple-image radiography. Med. Phys. 33, 278–289.

Chapman, D., Pisano, E., Thomlinson, W., Zhong, Z., Johnston, R.E., Washburn, D., Sayers, D., 1998. Medical and biological applications of diffraction enhanced imaging. Breast Dis. 10, 197–207.

Chapman, D., Thomlinson, W., Johnston, R.E., Washburn, D., Pisano, E., Gmür, N., Zhong, Z., Menk, R., Arfelli, F., Sayers, D., 1997. Diffraction enhanced X-ray imaging. Phys. Med. Biol. 42, 2015–2025.

Chou, C., Anastasio, M., Brankov, J., Wernick, M., Brey, E., Connor Jr., D., Zhong, Z., 2007. An extended diffraction-enhanced imaging method for implementing multiple-image radiography. Phys. Med. Biol. 52, 1923–1945.

Connor, D., Sayers, D., Sumner, D., Zhong, Z., 2006. Diffraction enhanced imaging of controlled defects within bone, including bone–metal gaps. Phys. Med. Biol. 51, 3283–3300.

Fitzgerald, R., 2000. Phase-sensitive X-ray imaging. Phys. Today 53, 23–26.

Hasnah, M., Zhong, Z., Parham, C., Zhang, H., Chapman, D., 2007. Crystal tilt error and its correction in diffraction enhanced imaging system. Nucl. Instrum. Methods A 572, 953–957.

Hasnah, M., Chapman, D., 2008. Alternative method of diffraction-enhanced imaging. Nucl. Instrum. Methods A 584, 424–427.

Kelly, M., Beavis, R., Fourney, D., Schultke, E., Parham, C., Juurlink, B., Zhong, Z., Chapman, L., 2006. Diffraction-enhanced imaging of the rat spine. Can. Assoc. Radiol. J. 57, 204–210.

Kelly, M., Coupal, D., Beavis, R., Schultke, E., Romanchuk, K., Juurlink, B., Zhong, Z., Chapman, L., 2007. Diffraction-enhanced imaging of a porcine eye. Can. J. Ophthalmol. 42, 731–733.

Khelashvili, G., Brankov, J., Chapman, D., Anastasio, M., Yang, Y., Zhong, Z., Wernick, M., 2006. A physical model of multiple-image radiography. Phys. Med. Biol. 51, 221–236.

Kim, C., Bourham, M., Doster, J., 2006. A wide-beam X-ray source suitable for diffraction enhanced imaging applications. Nucl. Instrum. Methods A 566, 713–721.

Kiss, M.Z., Sayers, D.E., Zhong, Z., Parham, C., Pisani, E., 2004. Improved image contrast of calcifications in breast tissue specimens using diffraction enhanced imaging. Phys. Med. Biol. 49, 3427–3439.

Lewis, R.A., Hall, C.J., Hufton, A.P., Evans, S., Menk, R.H., Arfelli, F., Rigon, L., Tromba, G., Dance, D.R., Ellis, I.O., Evans., A., Jacobs, E., Pinder, S.E., Rogers, K.D., 2003. X-ray refraction effects: application to the imaging of the biological tissues. Br. J. Radiol. 76, 301–308.

Li., J., Zhong, Z., Lidtke, R., Kuettner, K.E., Peterfy, C., Aliyeva, E., Muehleman, C., 2003. Radiography of soft tissue of the foot and ankle with diffraction enhanced imaging. J. Ant. 202, 463–470.

Muehleman, C., Chapman, L.D., Kuettner, K.E., Rieff, J., Mollenhauer, J.A., Massuda, K., Zhong, Z., 2003. Radiography of rabbit articular cartilage with diffraction enhanced imaging. Anat. Rec. A. 272, 392–397.

Muehleman, C., Li, J., Zhong, Z., 2006a. Preliminary study on diffraction enhanced radiographic imaging for a canine model of cartilage damage. Osteoarthritis Cartilage 14, 882–888.

Muehleman, C., Li, J., Zhong, Z., Brankov, J., Wernick, M., 2006b. Multiple-image radiography for human soft tissue. J. Anat. 208, 115–124.

Oltulu, O., Zhong, Z., Hasnah, M., Wernick, M.N., Chapman, D., 2003. Multiple image radiography in diffraction enhanced imaging. J. Phys. D: Appl. Phys. 36, 2152–2156.

Rao, D., Akatsuka, T., Tromba, G., 2003a. Transmission images and evaluation of tomographic imaging based scattered radiation from biological materials using 10, 15, 20 and 25 keV synchrotron X-rays: an analysis in terms of optimum energy. AIP Proc. 705, 1364–1367.

Rao, D., Akatsuka, T., Tromba, G., 2003b. Images of soft bodied animals with external hard shell A 3D visualization of the embedded soft tissue. AIP Proc. 705, 1308–1311.

Rao, D.V., Yuasa, T., Akatsuka, T., Zhong, Z., Tromba, G., Takeda, T., 2005. X-ray CT and DEI images of the biological soft-tissue using synchrotron X-rays. In: Proceedings of the Eighth International Conference on X-ray Microscopy, 26–30th July, Egret, Himeji, Japan, Sponsored by XRM 2005, pp. 233–234.

Rao, D.V., Zhong, Z., Tromba, G., 2007. Utilization of diffraction-enhanced imaging technique for soft-tissue imaging. In: Proceedings of the 15th International Conference on Vacuum Ultraviolet Radiation Physics, July 29th–August 3rd, 2007, Berlin, Germany. Book of Proceedings of Abstracts: Imaging and Microscopy, p 65.

Wernick, M., Yang, Y., Mondal, I., Chapman, D., Hasnah, M., Parham, C., Pisano, E., Zhong, Z., 2006. Computation of mass–density images from X-ray refraction-angle images. Phys. Med. Biol. 51, 1769–1778.

Wilkins, S.W., Gureyev, T.E., Gao, D., Pogany, A., Stevenson, A.W., 1996. Phase-contrast imaging using polychromatic hard X-rays. Nature 384, 335–338.

Young, L.W., Parham, C., Zhong, Z., Chapman, D., Reaney, M.J.T., 2007. Non-destructive diffraction enhanced imaging of seeds. J. Exp. Bot. 58 (10), 2513–2523.

Zhong, Z., Chapman, D., Menk, R., Richardson, J., Theophanis, S., Thomlinson, W., 1997. Monochromatic energy-subtraction radiography using a rotating anode source and a bent Laue monochromator. Phys. Med. Biol. 42, 1751–1762.

Zhong, Z., Thomlinson, W., Chapman, D., Sayers, D., 2000. Implementation of diffraction-enhanced imaging experiments at the NSLS and APS. Nucl. Instrum. Methods A 450, 556–567.